Rational Design of a Low-Cost, High-Performance Metal-Organic Framework for Hydrogen Storage and Carbon Capture

Matthew Witman,[†,⊥] Sanliang Ling,[‡,⊥] Andrzej Gladysiak,[¶] Kyriakos C. Stylianou,[¶] Berend Smit,[†,¶] Ben Slater,[‡] and Maciej Haranczyk[*,§,‖]

†*Department of Chemical and Biomolecular Engineering, University of California, Berkeley 94720, USA*

‡*Department of Chemistry, University College London, 20 Gordon Street, London WC1H 0AJ, UK*

¶*Laboratory of Molecular Simulation, Institut des Sciences et Ingénierie Chimiques, Valais, Ecole Polytechnique Fédérale de Lausanne (EPFL), Rue de l Industrie 17, CH-1951 Sion, Switzerland*

§*Computational Research Division, Lawrence Berkeley National Laboratory, Berkeley, California 94720, USA*

‖*IMDEA Materials Institute, C/Eric Kandel 2, 28906 - Getafe, Madrid, Spain*

⊥*Contributed equally to this work*

E-mail: mharanczyk@lbl.gov

Additional computational details

For all periodic density functional theory (DFT) calculations using CP2K, we employed double-ζ polarization quality Gaussian basis sets[1] and a 600 Ry plane-wave cutoff for the auxiliary grid, in conjunction with the Goedecker-Teter-Hutter pseudopotentials.[2,3] For hybrid DFT calculations, we have used cpFIT3 quality auxiliary basis sets for the Hartree-Fock exchange (HFX) calculations based on the auxiliary density matrix method (ADMM) approach,[4] and a cutoff radius of 4 Å for the HFX calculations using the truncated Coulomb potential.[5] Structural optimizations, including atomic coordinates and cell parameters, and total energy calculations of the periodic systems, were performed at density functional theory level, using both PBE[6] and PBE0[7,8] functionals, together with Grimme's D3 van der Waals correction with the Axilrod-Teller-Muto three-body terms.[9] A convergence threshold of 5.0 $\times$ 10^{-6} Hartree was used for all self-consistent field (SCF) calculations. The structural optimizations were considered converged if the maximum force on all atoms falls below 0.534 kcal mol^{-1} Å^{-1} (4.5 $\times$ 10^{-4} Hartree Bohr^{-1}). Majority of the calculations were performed with the Γ-point approximation using a 1 $\times$ 1 $\times$ 2 multiplication of the hexagonal primitive cell. Additional calculations were performed in a 1 $\times$ 1 $\times$ 3 supercell to check the convergence of the binding geometries and energies with respect to the supercell sizes. The counterpoise method[10] was used to correct for basis set superposition errors (BSSEs) in all binding energy calculations.

Periodic density functional theory (DFT) calculations of the vibrational frequencies and elastic constants of Mg_2(DHFUMA) were performed using Crystal with the B3LYP functional, in a rhombohedral cell with a total of 6 symmetry-inequivalent atoms. Monkhorst-Pack k-point grids of (8 $\times$ 8 $\times$ 8) were used to sample the Brillouin zone. Gaussian-type basis sets of 8-511d1G, 8-411d11G and 6-311d11G qualities were used for Mg, O and C, respectively. The accuracy of the integral calculations (i.e. the TOLINTEG keyword) were set to "7 7 7 7 16", and the "XLGRID" setting (i.e. extra large predefined grid) was used for the numerical integration of the exchange-correlation term. The vibrational frequencies

calculations were performed at the Γ-point, and the default displacement of 0.001 Å on each atom was used to compute the numerical second derivatives of the total energy. For the calculation of the elastic constants, we have used the default settings on size of lattice deformation (0.01 Å) and number of points (i.e. 3, including the central point with zero displacement) for the numerical second derivatives calculations. We have used the default energy and force convergence criteria for vibrational frequency and elastic constants calculations as defined by Crystal. These convergence criteria are typically tighter than separate single point and geometry optimization calculations.

Calculated vibrational frequencies of Mg_2(DHFUMA)

Table S1: Calculated vibrational frequencies (in cm^{-1}) of Mg_2(DHFUMA)

0.00	0.00	0.00	51.43	102.24	134.51
145.01	145.01	151.40	155.83	155.83	179.74
179.74	183.17	183.17	197.81	198.78	203.22
203.22	208.17	214.87	214.87	227.13	227.13
236.78	236.78	257.68	265.67	265.67	278.87
283.31	283.31	289.05	324.66	333.56	333.56
336.53	340.11	363.11	371.36	371.36	375.45
392.20	392.20	399.23	399.23	423.05	423.05
453.45	459.91	473.43	473.43	483.19	483.19
503.74	503.74	503.75	517.23	519.01	519.01
532.33	532.33	533.44	543.55	548.67	548.67
629.99	649.42	649.42	763.53	763.53	763.81
766.90	771.89	771.89	814.65	816.42	816.42
825.57	826.90	826.90	884.28	888.54	888.54
985.56	991.09	991.09	1186.45	1211.43	1211.43
1266.68	1279.78	1279.78	1358.82	1358.82	1417.73
1452.92	1454.46	1454.46	1550.64	1550.64	1553.73
1579.38	1579.38	1579.71	1608.71	1611.33	1611.33

Calculated elastic constants of Mg_2(DHFUMA)

Table S2: Calculated elastic constants (in GPa) of Mg_2(DHFUMA)

59.614	47.303	26.739	-0.522	6.763	0
	59.614	26.739	0.522	-6.763	0
		61.869	0	0	0
			38.422	0	-6.763
				38.422	-0.522
					6.155

Only the upper triangular part of the symmetric elastic matrix is shown. Our calculated elastic constants satisfy all the *necessary and sufficient* Born stability conditions[11] as derived by Mouhat and Coudert[12] for a rhombohedral (II) system (Laue class $\bar{3}$):

$C_{11} > |C_{12}|$

$C_{44} > 0$

$C_{13}^2 < \frac{1}{2}C_{33}\,(C_{11} + C_{12})$

$C_{14}^2 + C_{15}^2 < \frac{1}{2}C_{44}\,(C_{11} - C_{12}) \equiv C_{44}C_{66}$

Structure files and charges

The DFT optimized structures for Mg_2(DHFUMA) and Mg_2(DOBDC) are included in the structures.zip file. The partial atomic charges derived from the REPEAT analysis in all M_2(DOBDC) and M_2(DHFUMA) frameworks is presented in Table S3. Note that the labels of each atom type correspond to the atom types defined in the force field of Mercado *et al.* (see Figure S2).

Table S3: REPEAT derived partial charges for A = M_2(DHFUMA) and B = M_2(DOBDC)

Atom Type	M = Mg		M = Fe		M = Co		M = Ni		M = Zn	
	A	B	A	B	A	B	A	B	A	B
M	1.619	1.66	1.372	1.343	1.306	1.306	1.386	1.384	1.224	1.228
Oa	-0.952	-0.921	-0.908	-0.824	-0.869	-0.797	-0.926	-0.857	-0.779	-0.72
Ob	-0.734	-0.763	-0.722	-0.725	-0.711	-0.714	-0.713	-0.734	-0.648	-0.659
Oc	-0.781	-0.969	-0.679	-0.814	-0.633	-0.793	-0.681	-0.844	-0.604	-0.75
Ca	0.838	0.881	1.002	0.946	0.979	0.925	0.997	0.98	0.829	0.808
Cb	0.01	-0.316	-0.065	-0.373	-0.072	-0.341	-0.063	-0.388	-0.022	-0.283
Cc	—	0.478	—	0.444	—	0.415	—	0.443	—	0.377
Cd	—	-0.257	—	-0.205	—	-0.205	—	-0.191	—	-0.197
H	—	0.207	—	0.208	—	0.204	—	0.207	—	0.196

Additional crystallographic data for Mg_2(DHFUMA) and Mg_2(DOBDC)

Some additional crystallographic data for the DFT optimized Mg_2(DHFUMA) and Mg_2(DOBDC) structures are summarized in Table S4 for the reader's convenience. All quantities were computed in Zeo++ with high accuracy settings.

Table S4: Theoretical crystallographic data for Mg_2(DHFUMA) and Mg_2(DOBDC). Accessible quantities are computed for a probe radius of 1.65 Å

Property	Units	DHFUMA	DOBDC
Crystal density	[g/cm^3]	1.358	0.880
Cell volume	[Å^3/unit cell]	2120	4121
Accessible Surface Area	[m^2/g]	1043	1782
Accessible Surface Area	[m^2/cm^3]	1416	1568
Accessible Surface Area	[Å^2/unit cell]	272	646.3
Accessible Volume	[cm^3/g]	0.0945	0.350
Accessible Volume	[cm^3/cm^3]	0.130	0.308
Helium Void Fraction	[dimensionless]	0.484	0.716
Accessible Volume	[Å^3/unit cell]	272	1271
Largest Included Sphere	[Å]	7.6	11.8
Largest Free Sphere	[Å]	6.3	11.1

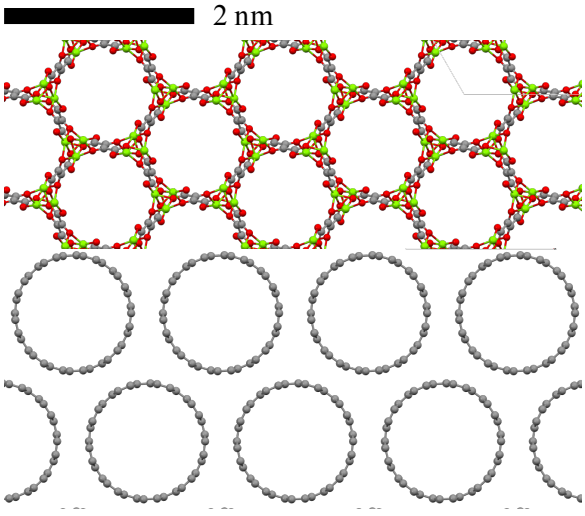

Figure S1: An segment of the periodic supercell of Mg_2(DHFUMA) is drawn to scale next to bundle of (n=5,m=5) SWNTs

We note that the channel geometry of Mg_2(DHFUMA), as well as each metal analog of

this framework, exhibits a striking similarity to the size and shape of carbon nanotubes. Figure S1 illustrates a to-scale representation of a periodic superlattice of Mg_2(DHFUMA) adjacent to a bundle of (n=5,m=5) single wall carbon nanotubes (SWNTs) which were generated by TubeGen Online [*http://turin.nss.udel.edu/research/tubegenonline.html*]. Yet the similarities between the two end with the pore shape and channel dimensionality, since the MOF structure has diverse chemical functionality (i.e. open metal sites) along the channel walls and the pore network is perfectly aligned in one dimension due to the chemical bonding between adjacent channels.

Force field parameterization details

All force field parameters and the polarizable model of Pham *et al.* were used to model H_2 adsorption in Mg_2(DHFUMA) and Mg_2(DOBDC).[13] Several minor differences exist between our RASPA2 simulation and the implementation of Pham et. al. that may describe the small discrepancy in the simulated isotherms for Mg_2(DOBDC). Firstly, the partial atomic charges of all framework atoms were taken from our REPEAT analysis (see Section) which are not identical to those of Pham *et al.* Secondly, we accounted for quantum nuclear effects by a second order Feynmann-Hibbs correction term to the Lennard-Jones potential (equation S1) as implemented in RASPA2, whereas Pham *et al.* used the fourth order correction term (equation S2). Thirdly, *et al.* utilize a modified dipole field tensor to damp dipole-dipole interactions that exhibit short range divergences. Finally, back polarization was not accounted for in our simulation. Our H_2 charges, H_2 Lennard-Jones parameters, framework Lennard-Jones parameters, and static point polarizabilities were identical to Pham *et al.*

$$U_{FH} = U + \frac{\beta\hbar^2}{24\mu}(U'' + \frac{2}{r}U') \tag{S1}$$

$$U_{FH} = U + \frac{\beta\hbar^2}{24\mu}(U'' + \frac{2}{r}U') + \frac{\beta\hbar^4}{1152\mu^2}(U'''' + \frac{4}{r}U''' + \frac{15}{r^3}U') \tag{S2}$$

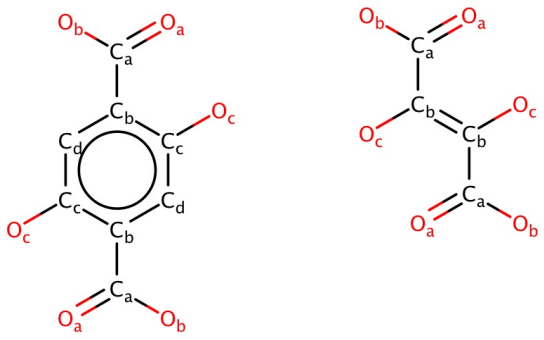

Figure S2: Atom types assigned for DOBDC ligand as defined by Mercado's FF (left) and atom types assigned for DHFUMA ligand (right) in this work.

For modeling H_2O and CO_2 in the M_2(DHFUMA) and M_2(DOBDC) series, the Buckingham potential and force field parameters of Mercado et. al. were used.[14] We refer the reader to this publication for all force field parameters and details on its derivation and implementation. Each atom type in the DHFUMA ligand was assigned the analogous type to the DOBDC ligand, shown in Figure S2.

CO_2 force field transferability

Force field parameterizations of adsorbate interactions in nanoporous materials are often validated by their ability to reproduce *ab initio* or experimentally determined adsorbate binding energies and configurations. The agreement in the simulated binding energy between our *ab initio* calculations and the parameterized classical force field of Mercado et. al. is shown in Table S5.

Table S5: *Ab initio* vs classical calculation of CO_2 binding energies [kJ/mol] in M_2(DOBDC) and M_2(DHFUMA) structures

Metal	DHFUMA			DOBDC		
	Ab. init.	FF	% Diff.	*Ab. init.*	FF	% Diff.
Mg	-50.1	-54.6	5	-41.3	-43.3	9
Fe	-40.9	-47.0	19	-30.0	-35.8	14
Co	-41.1	-49.8	16	-29.3	-34.1	21
Ni	-46.1	-49.1	5	-34.8	-36.5	6
Zn	-37.6	-39.1	1	-31.3	-31.7	4

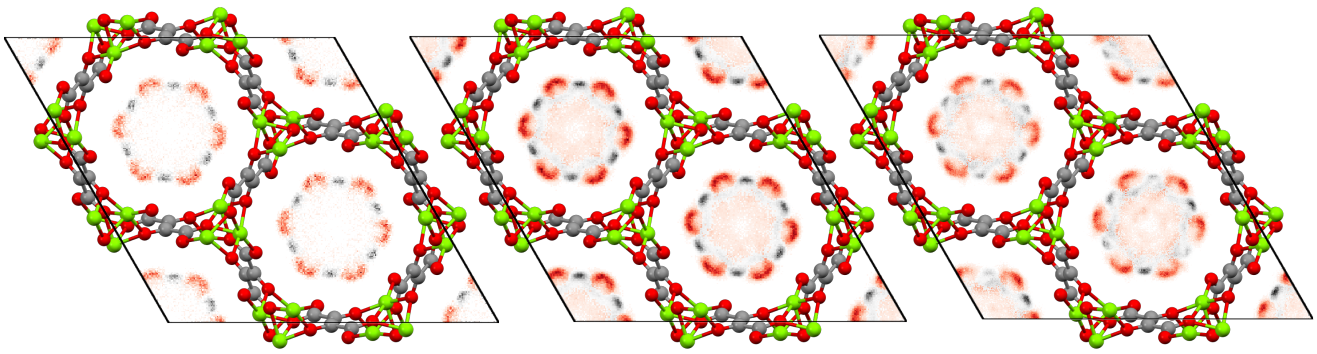

Figure S3: Two dimensional elemental probability density plots of CO_2 taken from snaphsots throughout a GCMC simulation at 313 K at approximate loadings of (a) 1 CO_2 molecule per unit cell; (b) 9 molecules per unit cell which corresponds to 0.5 molecules per open metal site; and (c) 15 molecules per unit cell which corresponds to saturation loading. Black represents Carbon and red represents Oxygen. The element with the higher normalized probability of occupation at that particular pixel determines the coloring.

This agreement is particularly important for accurate computation of gas adsorption behavior in the Henry and low-pressure regimes which are the most important regimes for CO_2 adsorption in the DHFUMA analog series. All DHFUMA analogs display significantly

stronger binding than their DOBDC counterpart, a direct result of the optimized binding geometry afforded by the proximity of adjacent open metal sites. The same binding geometry is observed in the CO_2 probability density map generated by extracting various snapshots of adsorbate configurations throughout the course of a GCMC in Mg_2(DHFUMA). These probability density maps are shown in Figure S3 and demonstrate that an Oxygen atom is most likely to be adjacent to an open metal site, whereas Carbon is most likely to be found directly between two Oxygens which are each bound to an open metal site. This agreement of CO_2 binding energies and binding geometries between classical GCMC simulations and *ab intio* simulations suggests that Mercado *et al.*ś classical force field parameterization is indeed transferable to this system and can reasonably reproduce the *ab initio* potential energy surface of CO_2 in the DHFUMA system.

CO_2 insotherms for M_2(DHFUMA) and M_2(DOBDC) [M = Mg, Fe, Co, Ni, Zn]

GCMC computed (T = 313 K and T = 400 K) CO_2 isotherms for all metal analogs of the DOBDC and DHFUMA variants of MOF-74 are presented, plotted in units of molecules CO_2 per unit cell and moles CO_2 per kg framework on normal-normal and log-log scales. The log-log plots particularly demonstrate the enhanced CO_2 uptake in the Henry and low-pressure regimes.

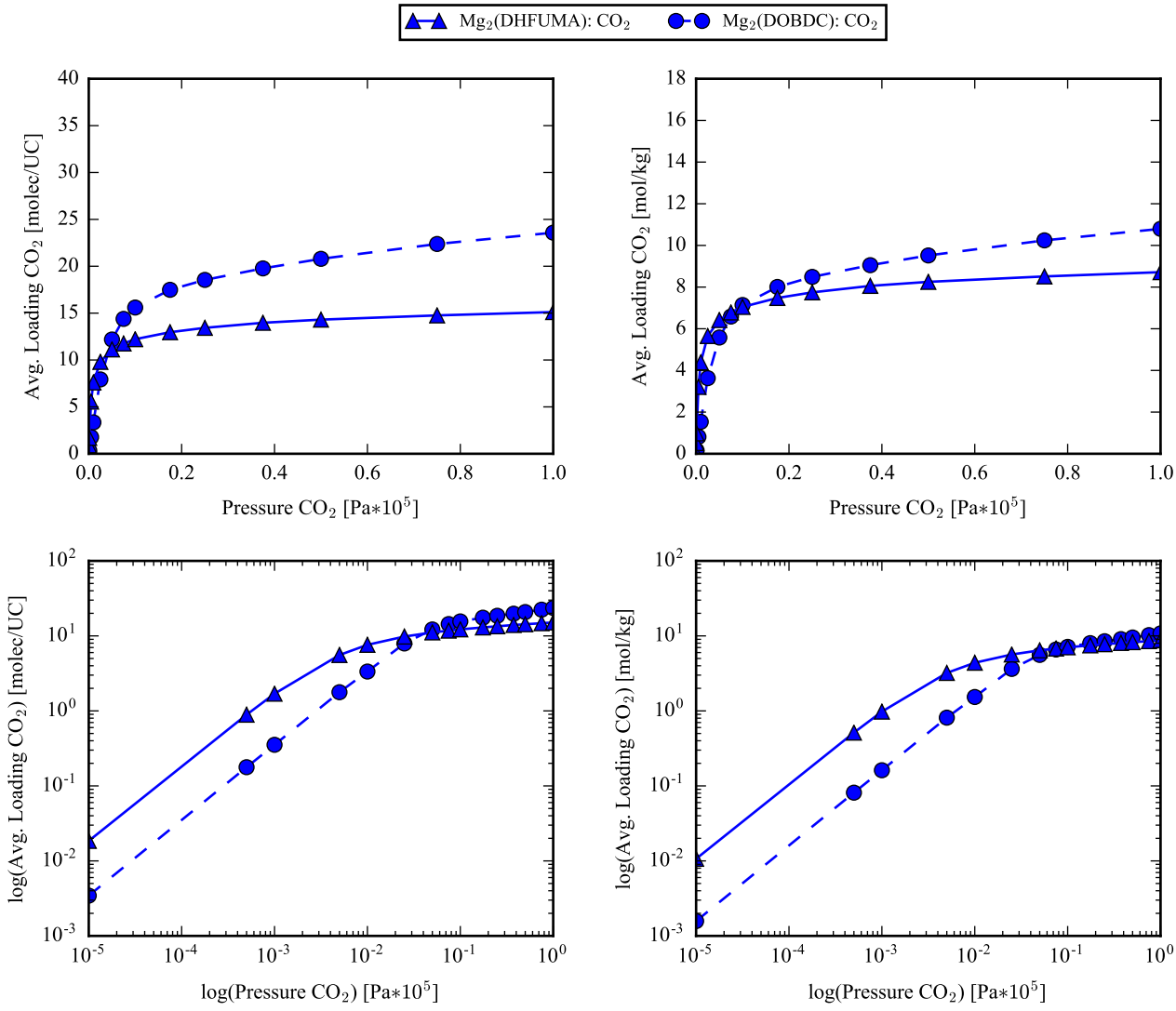

Figure S4: CO_2 isotherms at T = 313 K for Mg_2(DOBDC) and Mg_2(DHFUMA) variants

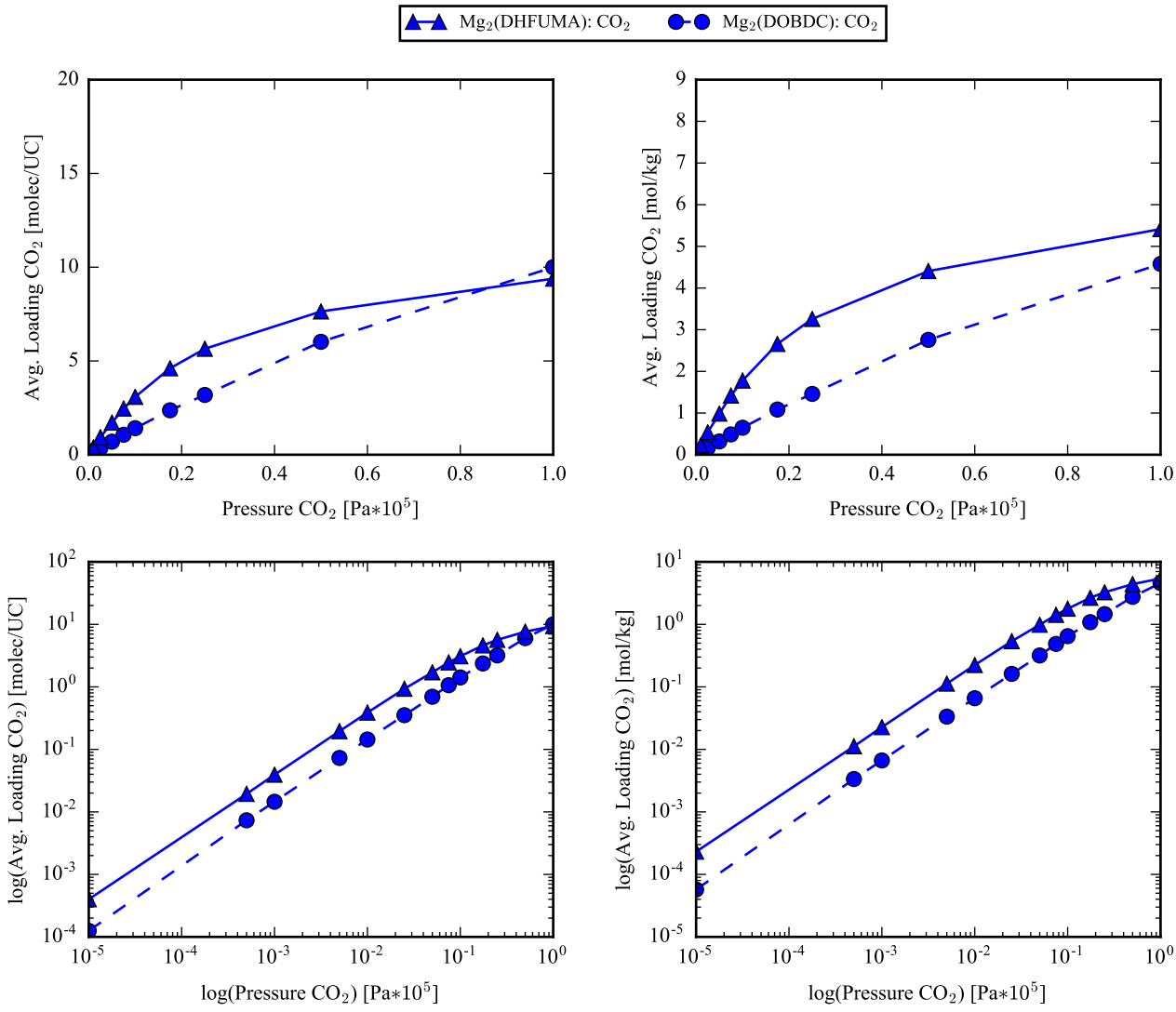

Figure S5: CO_2 isotherms at T = 400 K for Mg_2(DOBDC) and Mg_2(DHFUMA) variants

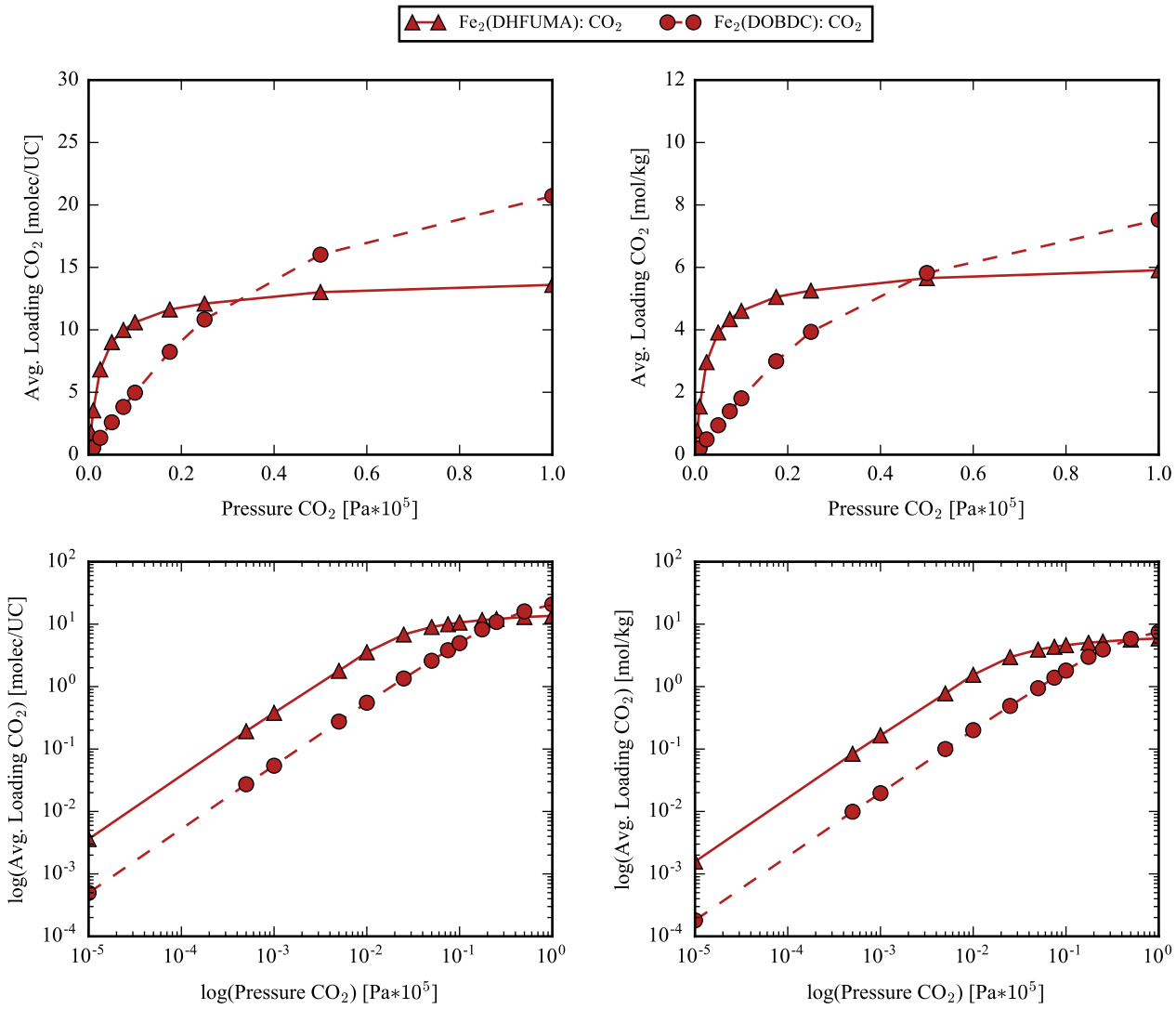

Figure S6: CO_2 isotherms at T = 313 K for Fe_2(DOBDC) and Fe_2DHFUMA variants

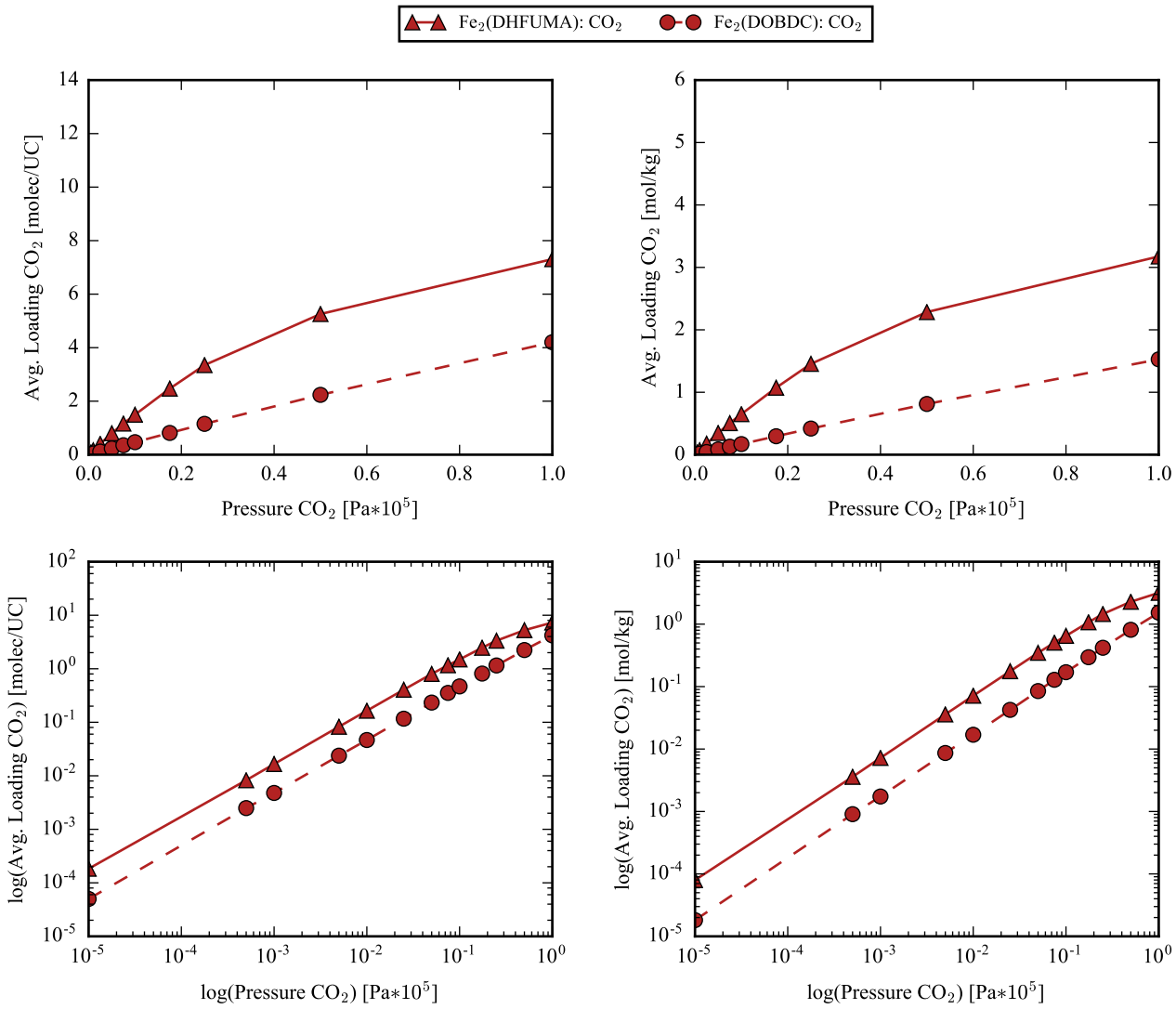

Figure S7: CO_2 isotherms at T = 400 K for Fe_2(DOBDC) and Fe_2DHFUMA variants

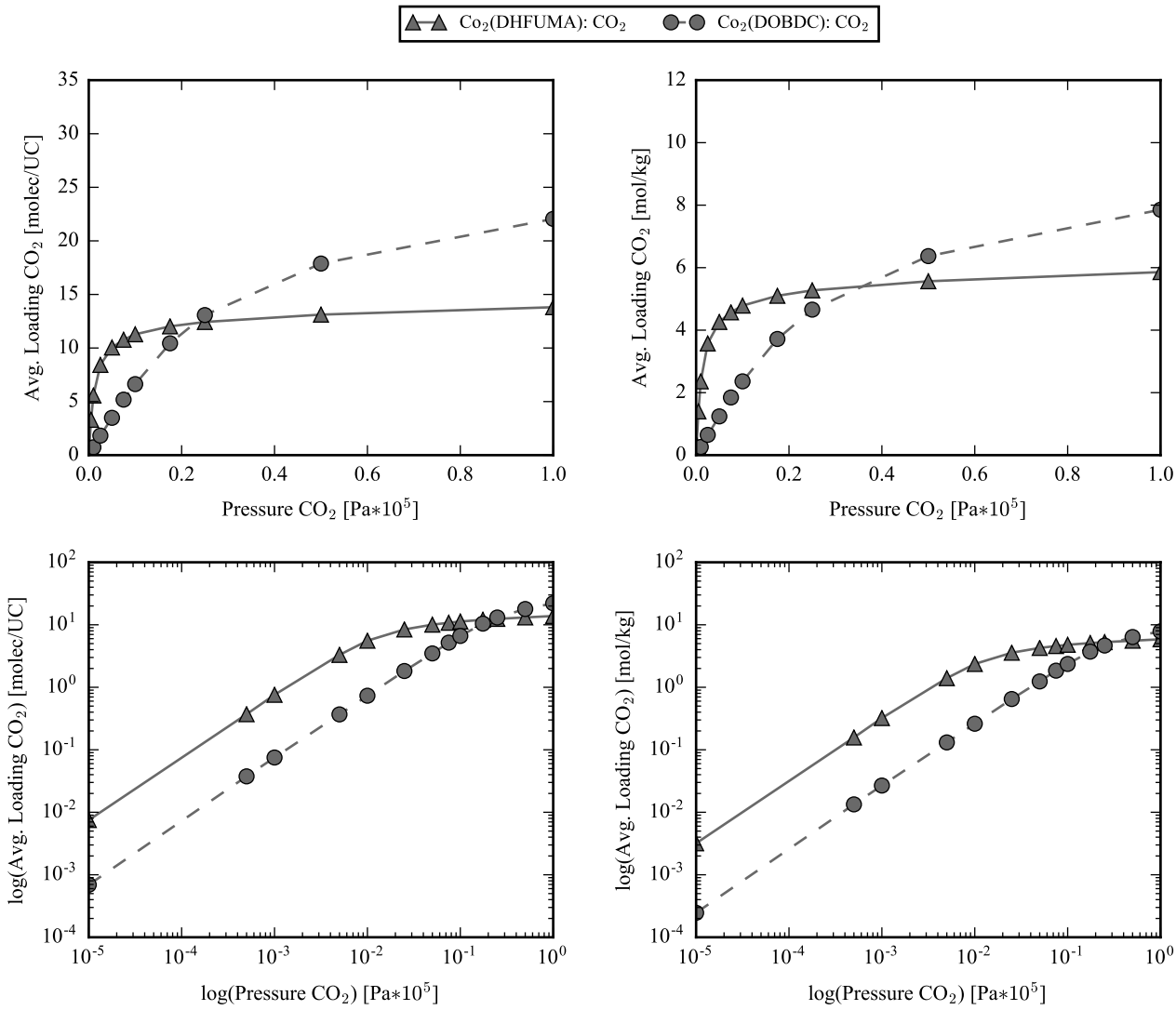

Figure S8: CO_2 isotherms at T = 313 K for Co_2(DOBDC) and Co_2(DHFUMA) variants

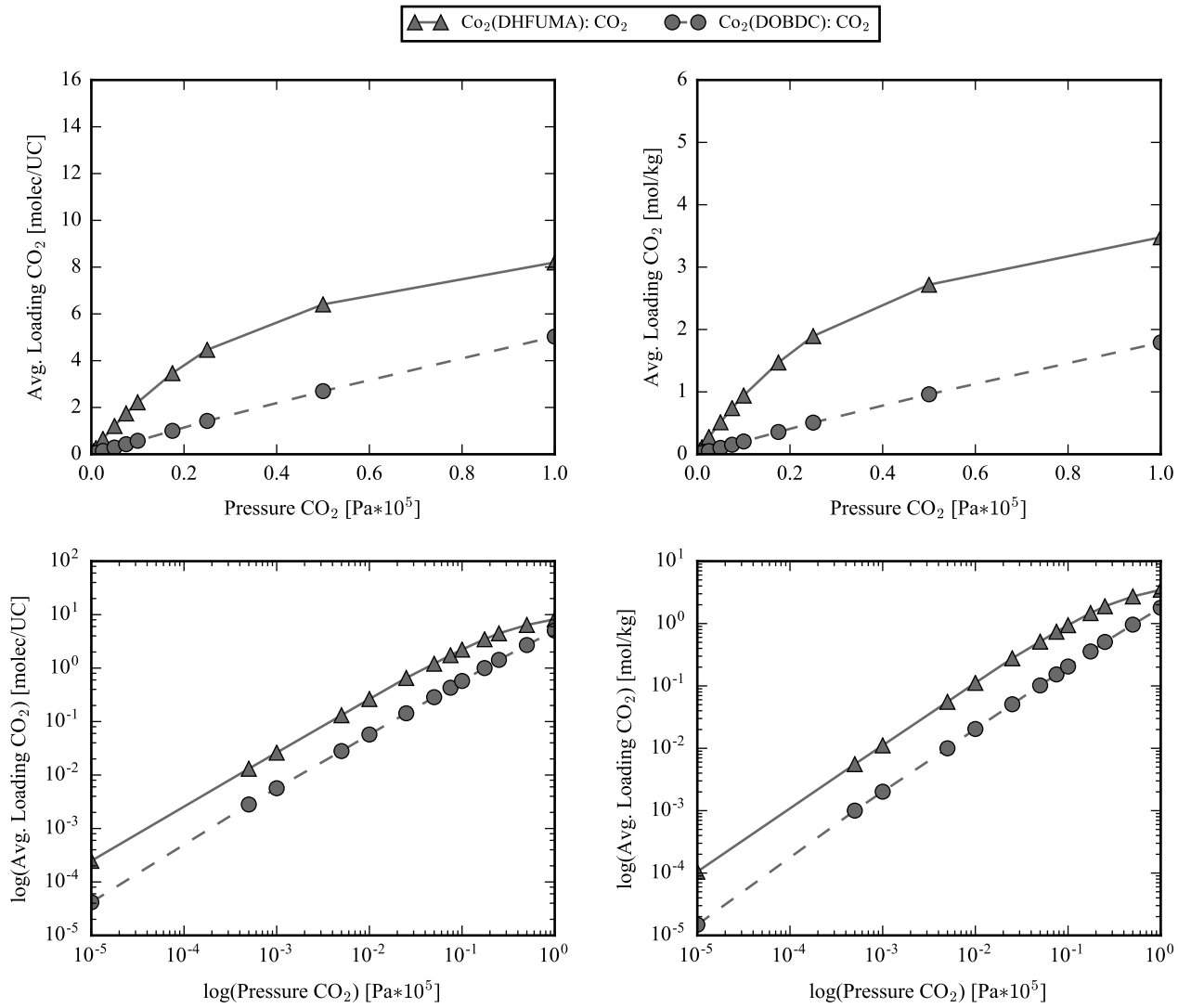

Figure S9: CO_2 isotherms at T = 400 K for Co_2(DOBDC) and Co_2(DHFUMA) variants

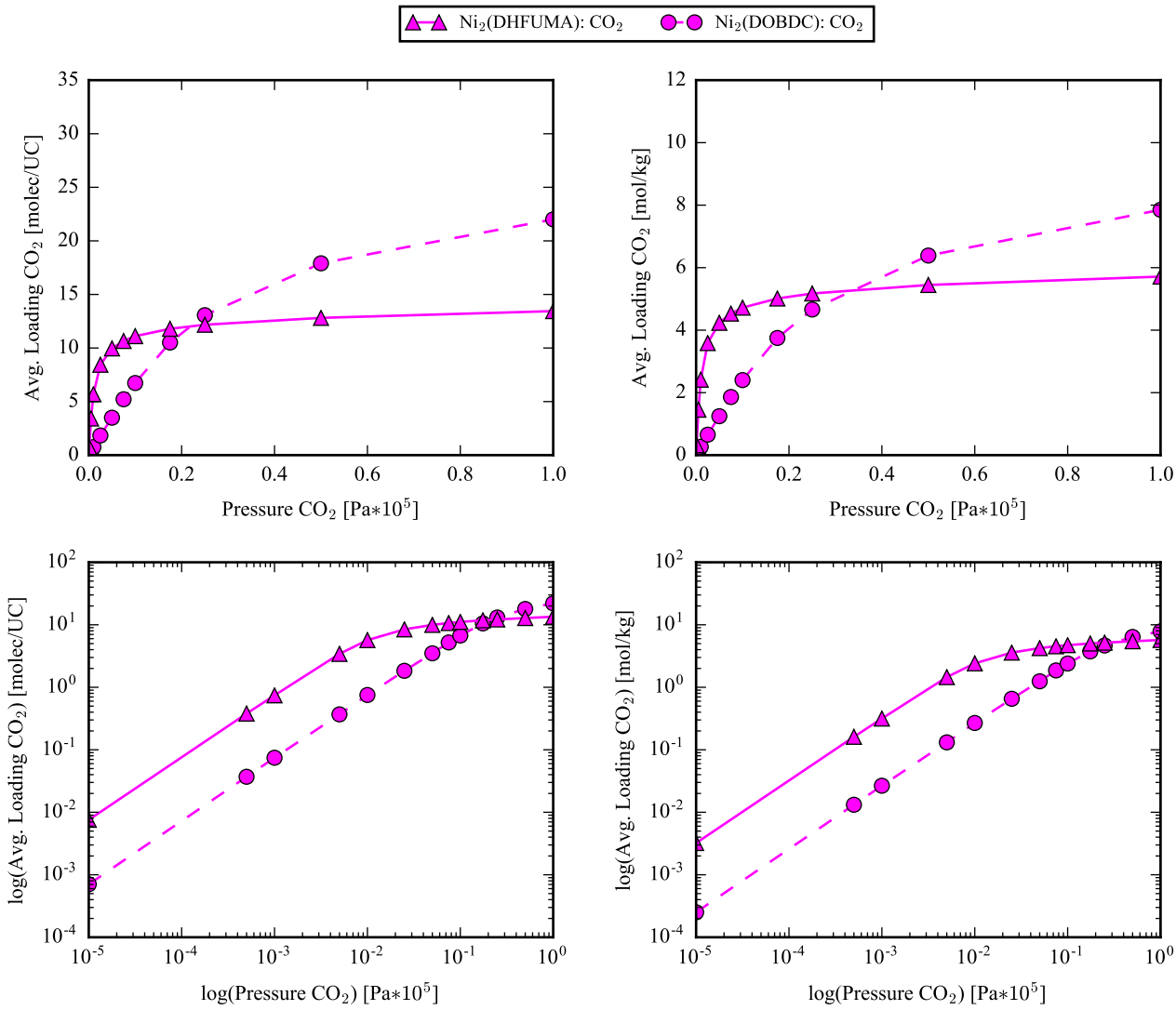

Figure S10: CO_2 isotherms at T = 313 K for Ni_2(DOBDC) and Ni_2(DHFUMA) variants

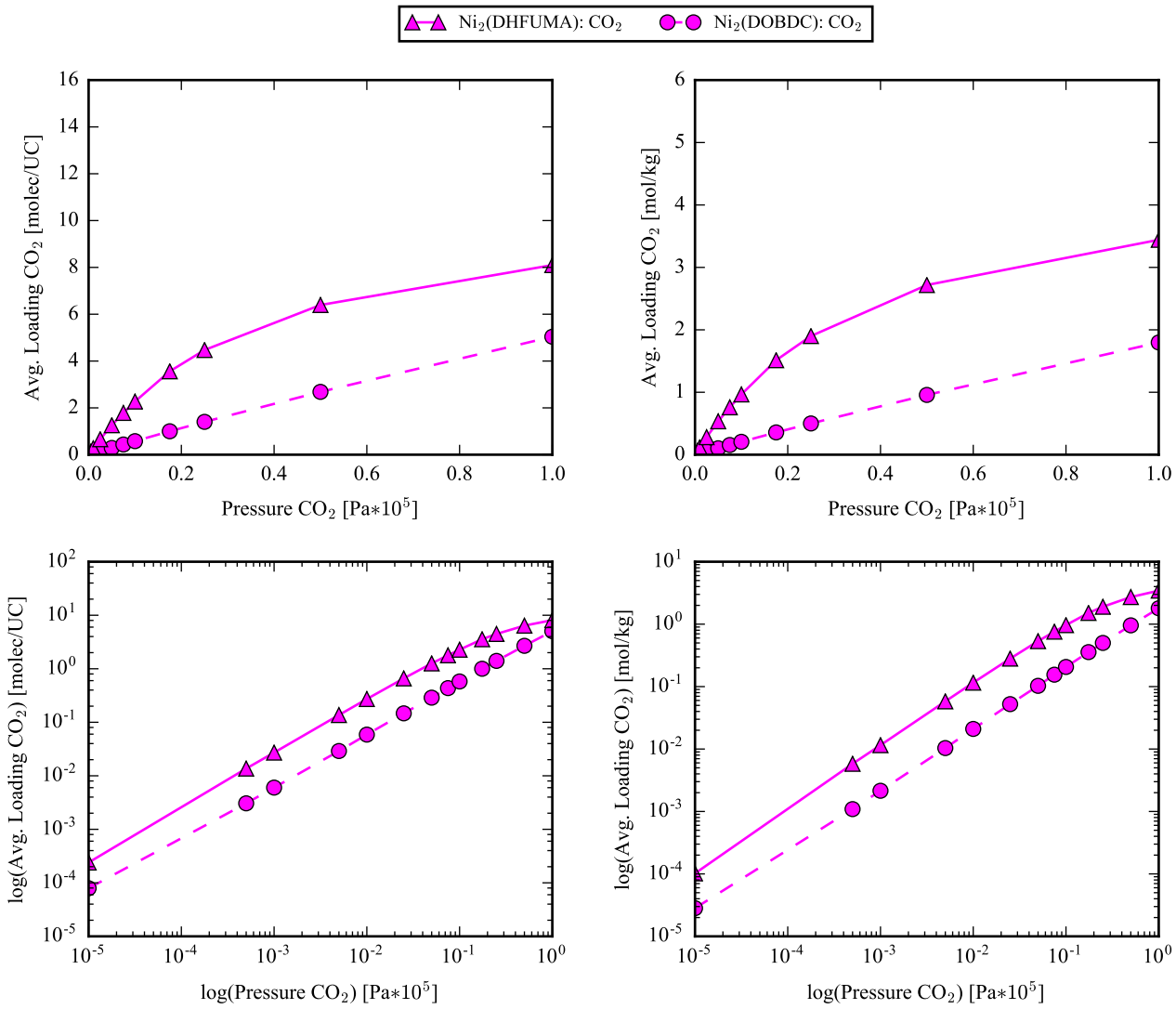

Figure S11: CO_2 isotherms at T = 400 K for Ni_2(DOBDC) and Ni_2(DHFUMA) variants

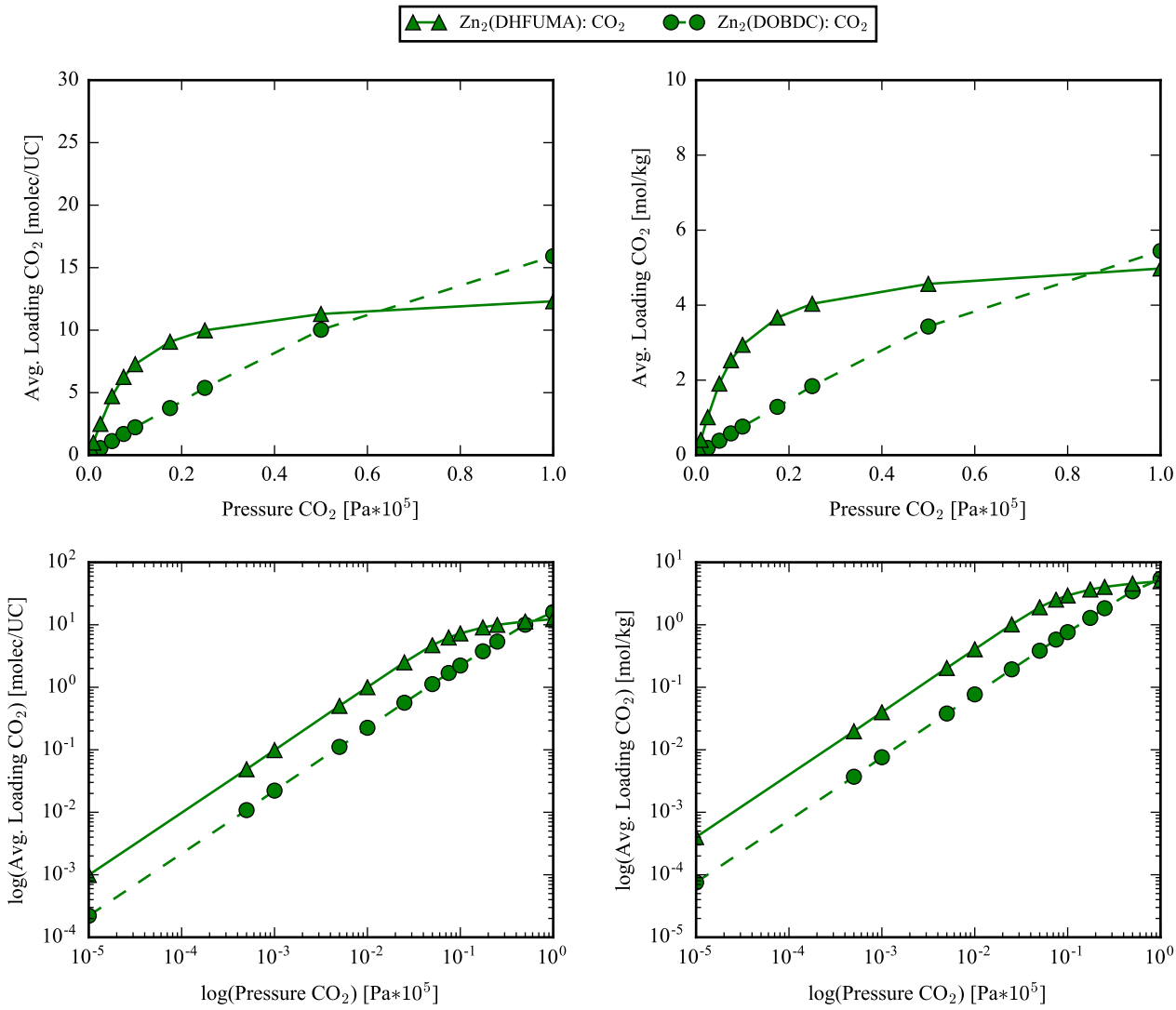

Figure S12: CO_2 isotherms at T = 313 K for Zn_2(DOBDC) and Zn_2(DHFUMA) variants

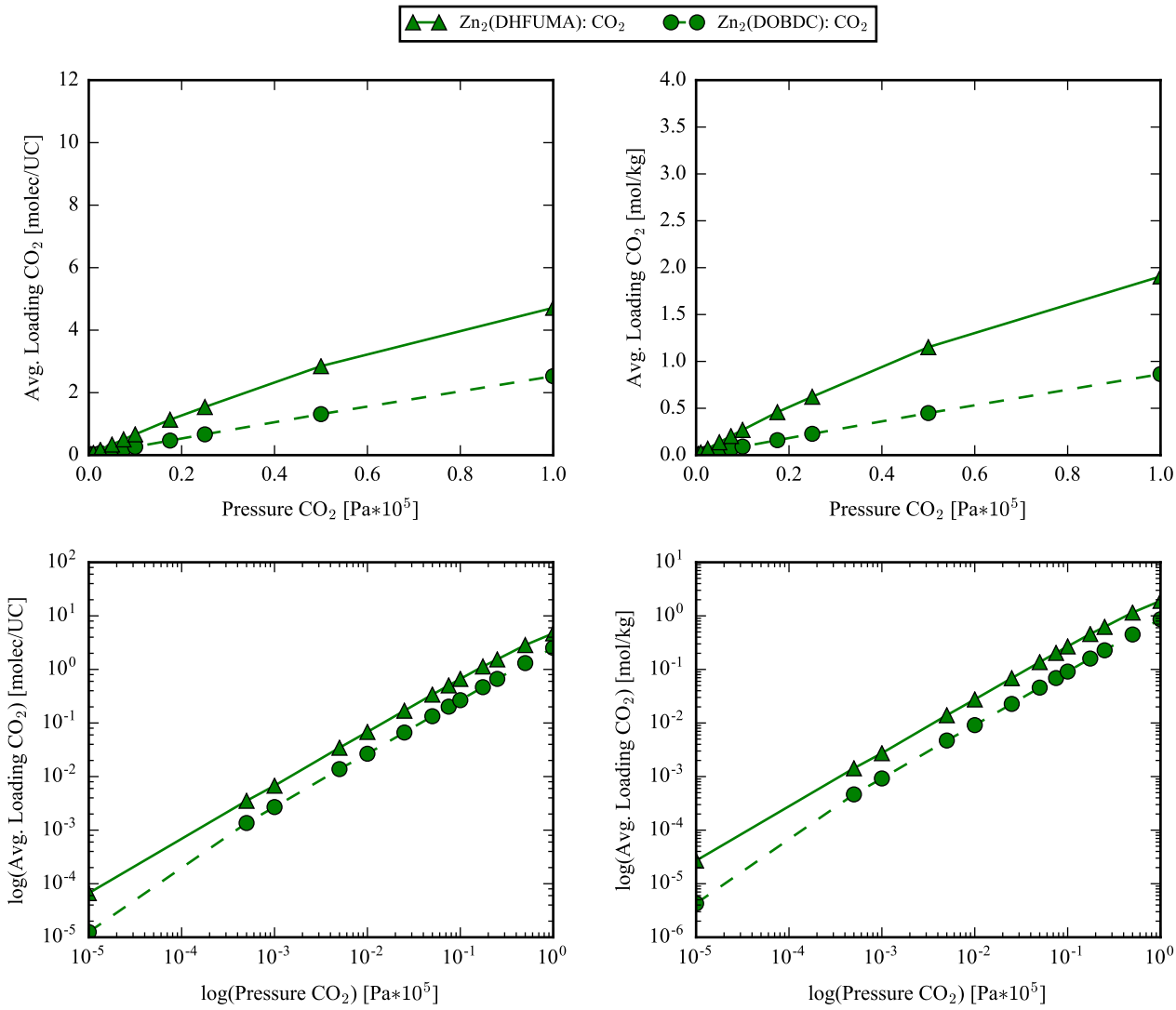

Figure S13: CO_2 isotherms at T = 400 K for Zn_2(DOBDC) and Zn_2(DHFUMA) variants

H_2O isotherms for M_2(DHFUMA) and M_2(DOBDC) [M = Mg, Fe, Co, Ni, Zn]

GCMC computed (T = 313.0 K and T = 400.0 K) H_2O isotherms for all metal analogs of the DOBDC and DHFUMA variants of MOF-74 are presented. While DHFUMA condenses H_2O at a much lower external pressure than DOBDC due to the reduced pore size, the condensation point can be dramatically increased by raising the reservoir temperature. For example, the condensation pressure in Mg_2(DHFUMA) increases by almost three orders of magnitude when increasing the reservoir temperature from T = 313 K to T = 400 K. It is worth noting that at a temperature of T = 400 K, a majority of the DHFUMA analogs exhibit water condensation in the H_2O partial pressure range that could be reasonably achieved by drying a typical coal-fired flue gas (on the order of 1 mol% H_2O).

By utilizing the force field of Mercado *et al.* we are able to simulate the adsorption of H_2O in the M_2(DOBDC) and M_2(DHFUMA) frameworks to obtain a reasonable estimate of the pressure at which the step in this isotherm occurs. We assume the H_2O force field parameters are transferable as is the case with CO_2, yet we note that accurate molecular simulation of water is a challenging feat and an ongoing topic of research for decades. Simulation of water in confined spaces (such as the channels of DOBDC and DHFUMA) is also extremely challenging and extremely dependent of water model and force field parameters, as evidenced by a dearth of agreements between experimental and theoretical results for water adsorption in zeolites, MOFs, etc.[15] We expect three major trends to exist in the water adsorption isotherms for M_2(DOBDC) and M_2(DHFUMA). Firstly, we expect the condensation to occur in DHFUMA analogs at a lower pressure than their DOBDC counterpart since the pore channel is smaller and enhanced cooperative adsorption is stronger. Secondly, we expect the metal with strongest H_2O binding energy to exhibit a step at the lowest H_2O pressure. This trend matches the DFT binding energies of H_2O with the exception of the reversal of Mg_2(DHFUMA) and Ni_2(DHFUMA). Thirdly, the H_2O pressure at which the adsorption

step occurs must increase with increasing temperature since higher temperatures shift the chemical potential of the external reservoir. Figure S14 demonstrates these three major trends that are at minimum qualitatively correct but in the best case would exactly reproduce the experimental adsorption trends across all metals in each structural series.

Despite the difficulties associated with molecular simulation of H_2O, Figure S14 demonstrates the the most important trend regarding our discussion of CO_2 adsorption in the presence of H_2O: high temperature adsorption increases the condensation pressure of H_2O in the M_2(DOBDC) and M_2(DHFUMA) frameworks.

The same binding configuration of H_2O is predicted by the Mercado force field and *ab intiio* calculations. Figure S15 shows the elemental probability density map of H_2O in Mg_2(DHFUMA) generated from snapshots throughout a GCMC simulation (P = 0.5 Pa, T = 313 K), which corresponds to an average loading of about 30 H_2O molecules/UC (or ∼1.5 molecules/Mg^{2+}). The density map clearly demonstrates that the dominant binding mode is that of one Oxygen per open metal site.

This configuration agrees closely with the binding geometry of H_2O as calculated from our DFT optimization, shown in Figure S16.

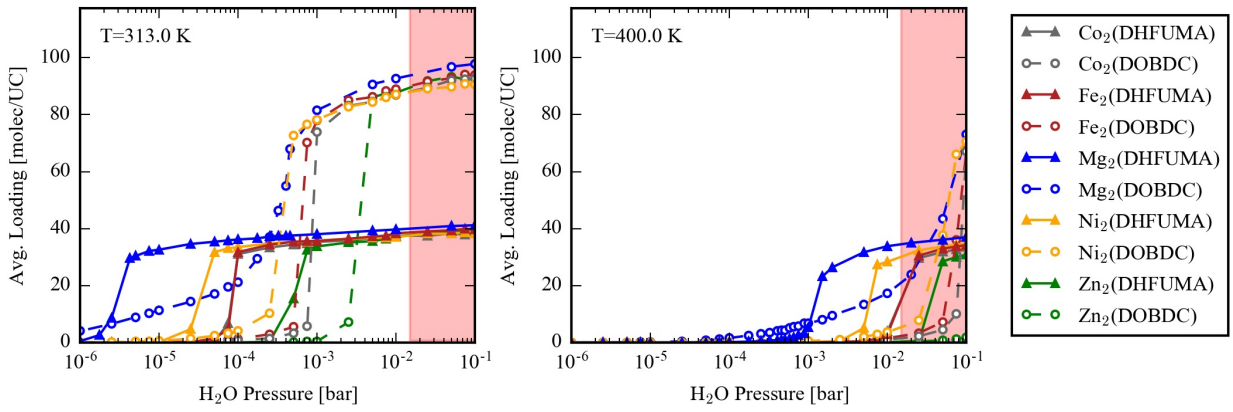

Figure S14: Absolute H_2O adsorption in M_2(DOBDC) and M_2(DHFUMA) at (a) 313 K and at (b) 400 K. The pressure region in red corresponds a broad partial pressure range of H_2O (P = ∼0.01-0.1 bar) that one might expect in the scrubbed exhaust gas from a coal fired power plant.

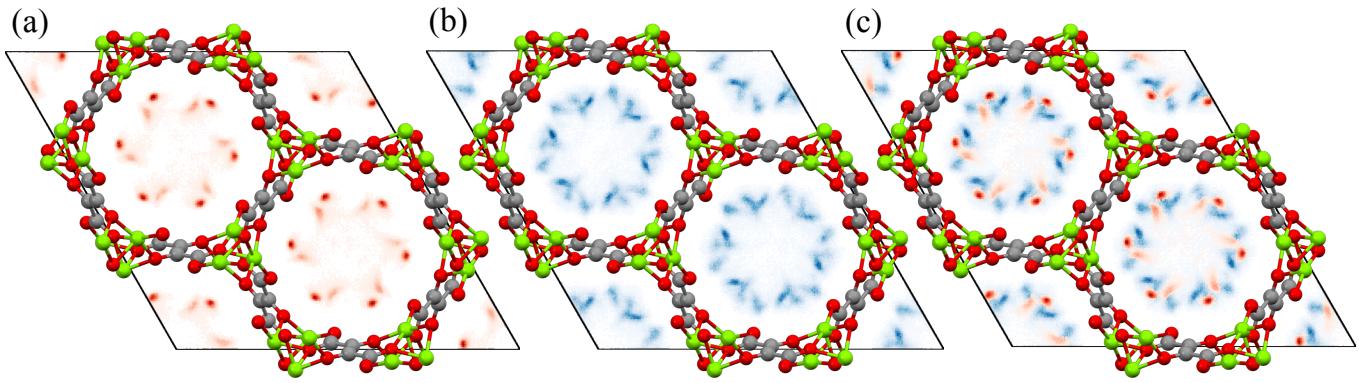

Figure S15: Elemental probability density maps of H_2O taken from snapshots of a GCMC simulation at P = 0.5 Pa and T = 313 K, which corresponds to an approximate loading of 30 molecules/UC or ∼1.5 molecules/M^{2+}. Shown is (a) the elmental proabability density of O alone; (b) the density of H alone; and (c) the density of both O and H overlayed where the coloring of each pixel is determined by the element with higher normalized probability of occupation at that grid point.

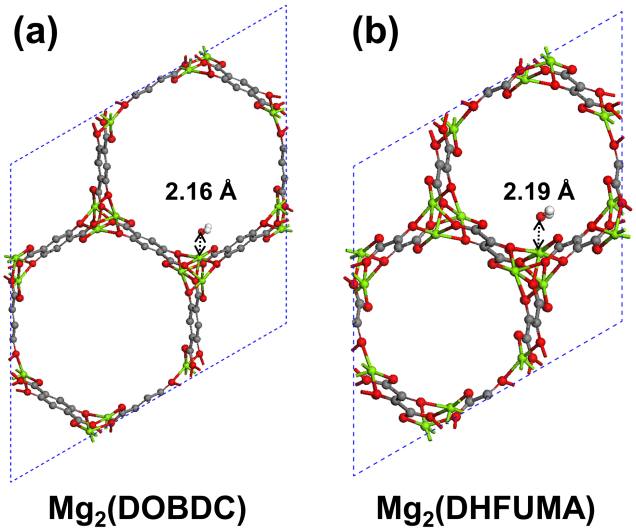

Figure S16: DFT optimised binding configurations of H_2O in (a) Mg_2(DOBDC) and (b) Mg_2(DHFUMA).

H_2O:CO_2 mixture analysis for M_2(DHFUMA) and M_2(DOBDC) [M = Mg, Fe, Co, Ni, Zn]

GCMC simulations of a binary H_2O:CO_2 mixture at fixed total pressure of P = 0.15 bar for all analogs at varying temperatures are summarized below. Each data point corresponds to a single GCMC simulation with 2-components. The molar ratio of H_2O:CO_2 is varied at constant total pressure to generate the mixture analysis for each structure at each temperature. A stepped decrease in the CO_2 equilibrium uptake occurs at a critical mole fraction of water (i.e. the critical pressure at which water condenses in the channels of each structure).

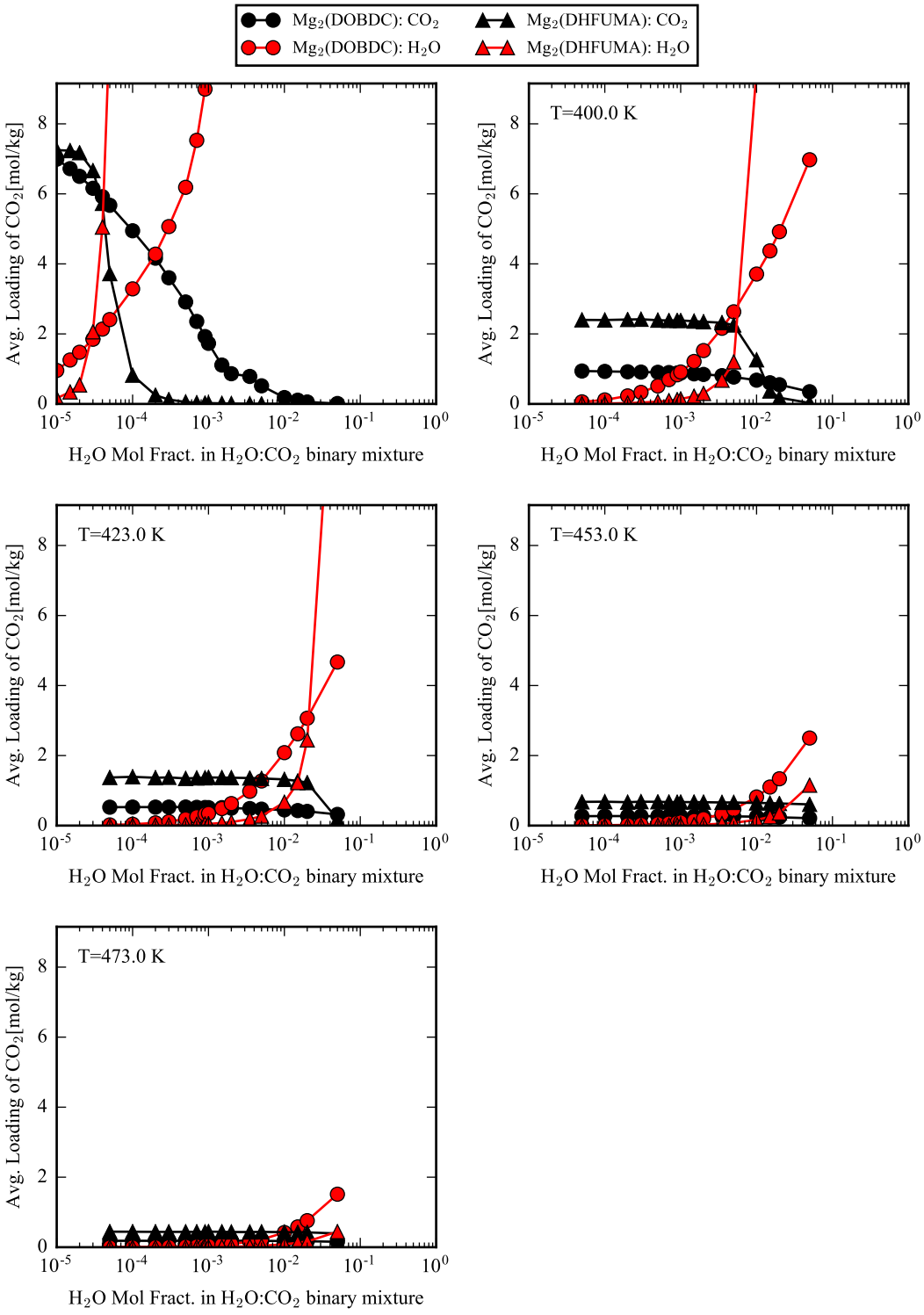

Figure S17: H_2O:CO_2 mixture analysis for all Mg analogs. Each data point corresponds to one GCMC simulation at P_{total} = 0.15 bar and each subplot corresponds to a fixed temperature of T = 313, 400, 423, 453, or 473 K where the molar composition of the H_2O:CO_2 mixture is varied.

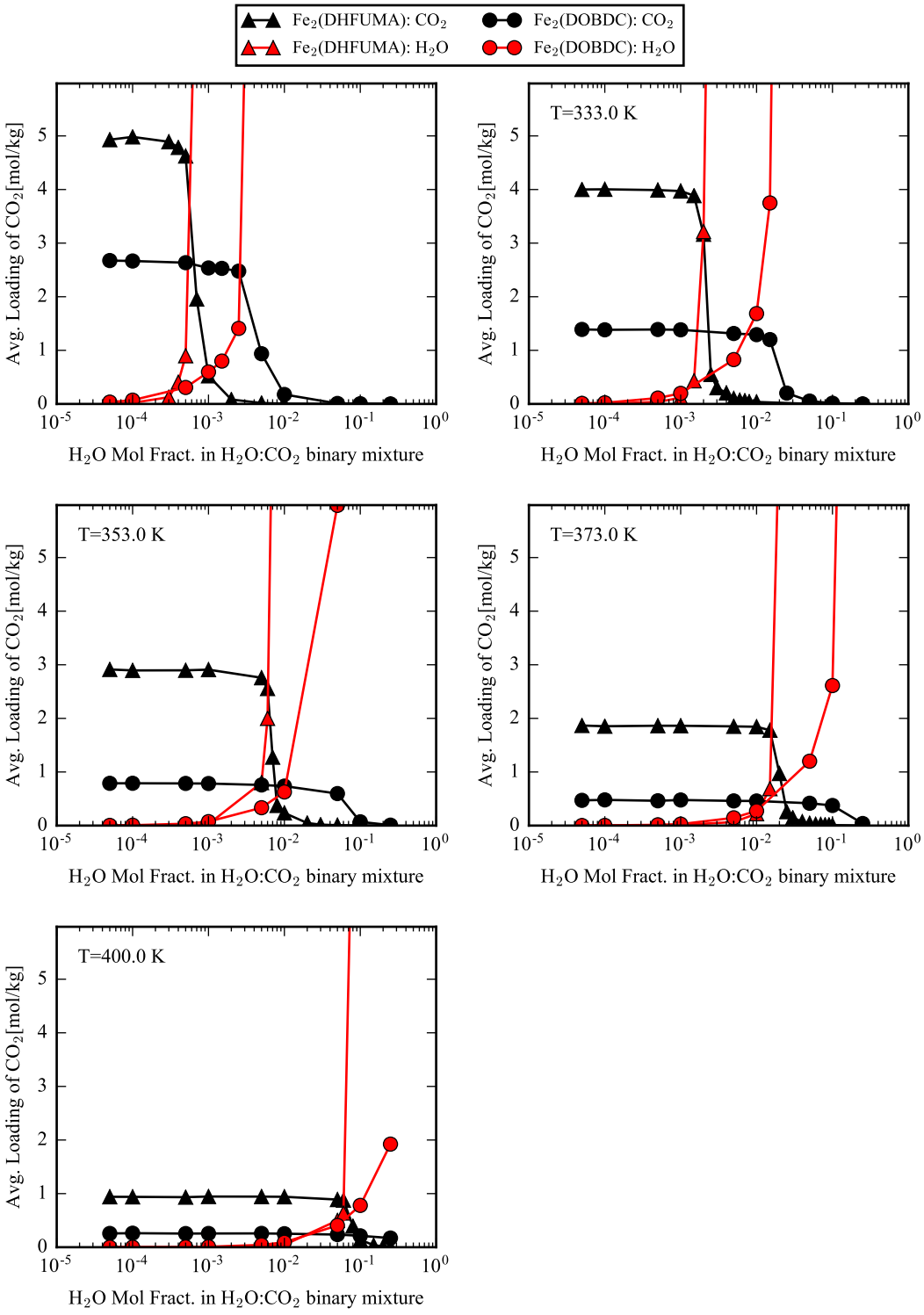

Figure S18: H_2O:CO_2 mixture analysis for all Fe analogs. Each data point corresponds to one GCMC simulation at P_{total} = 0.15 bar and each subplot corresponds to a fixed temperature of T = 313, 333, 353, 373, or 400 K where the molar composition of the H_2O:CO_2 mixture is varied.

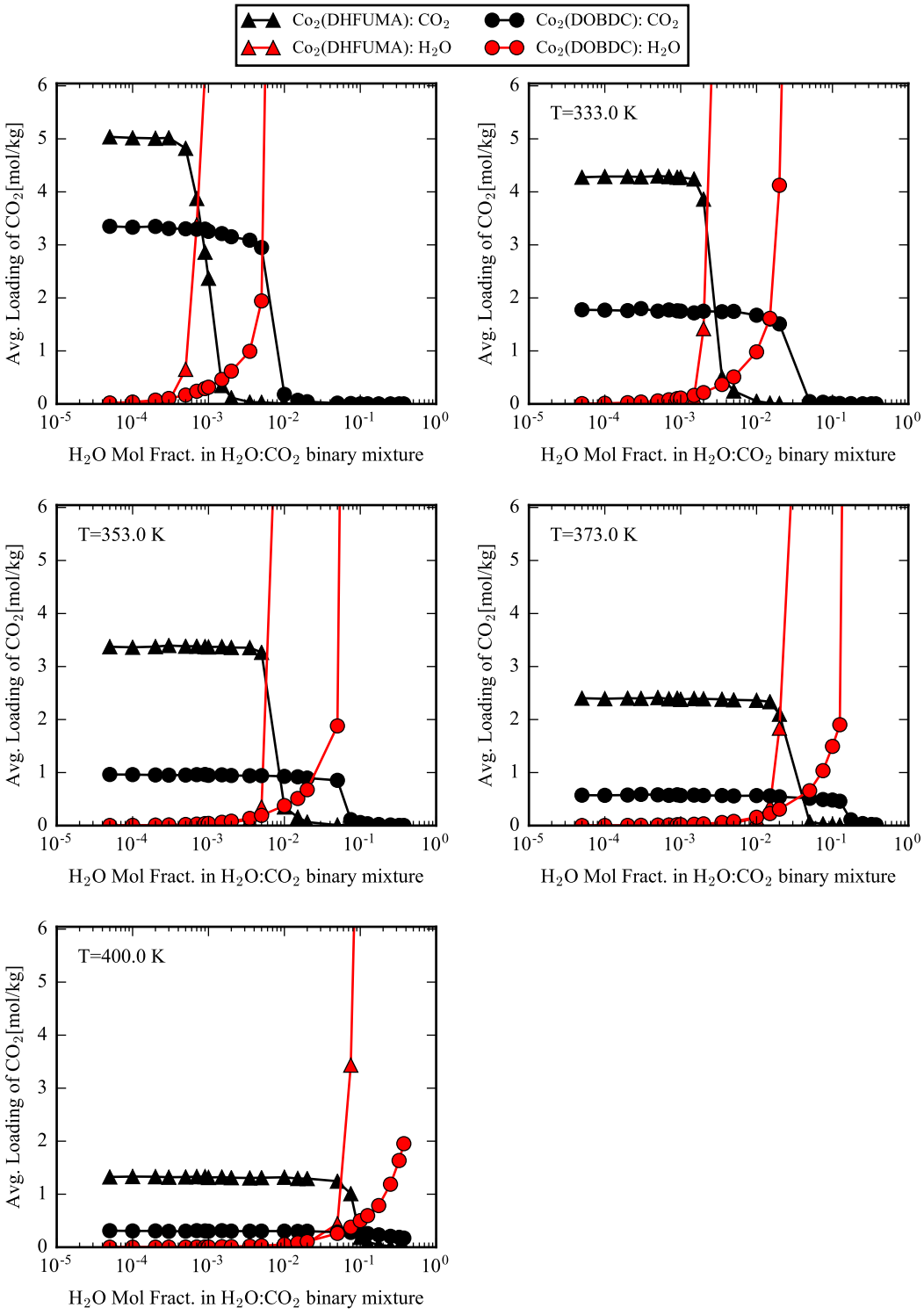

Figure S19: H_2O:CO_2 mixture analysis for all Co analogs. Each data point corresponds to one GCMC simulation at P_{total} = 0.15 bar and each subplot corresponds to a fixed temperature of T = 313, 333, 353, 373, or 400 K where the molar composition of the H_2O:CO_2 mixture is varied.

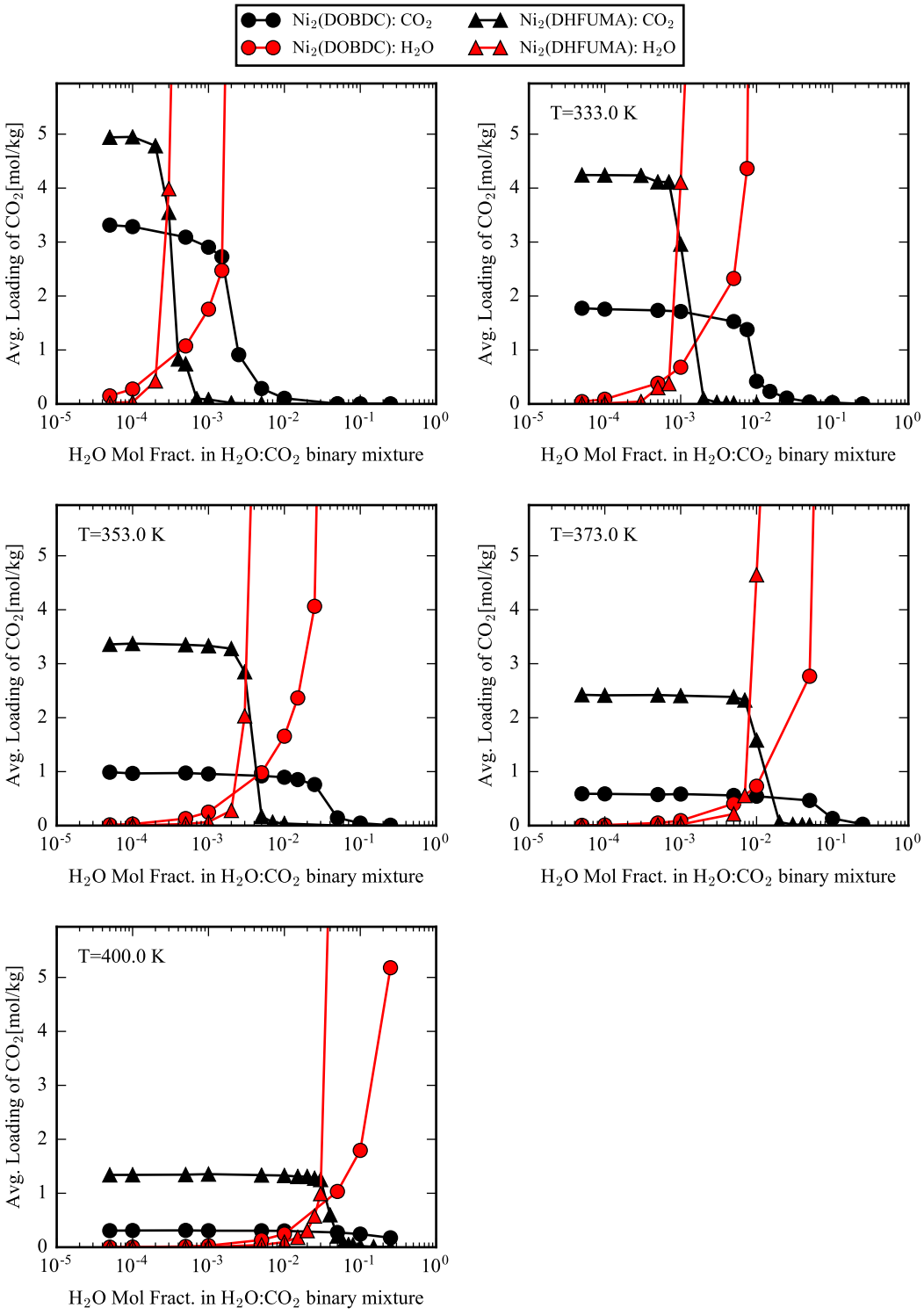

Figure S20: H_2O:CO_2 mixture analysis for all Ni analogs. Each data point corresponds to one GCMC simulation at P_{total} = 0.15 bar and each subplot corresponds to a fixed temperature of T = 313, 333, 353, 373, or 400 K where the molar composition of the H_2O:CO_2 mixture is varied.

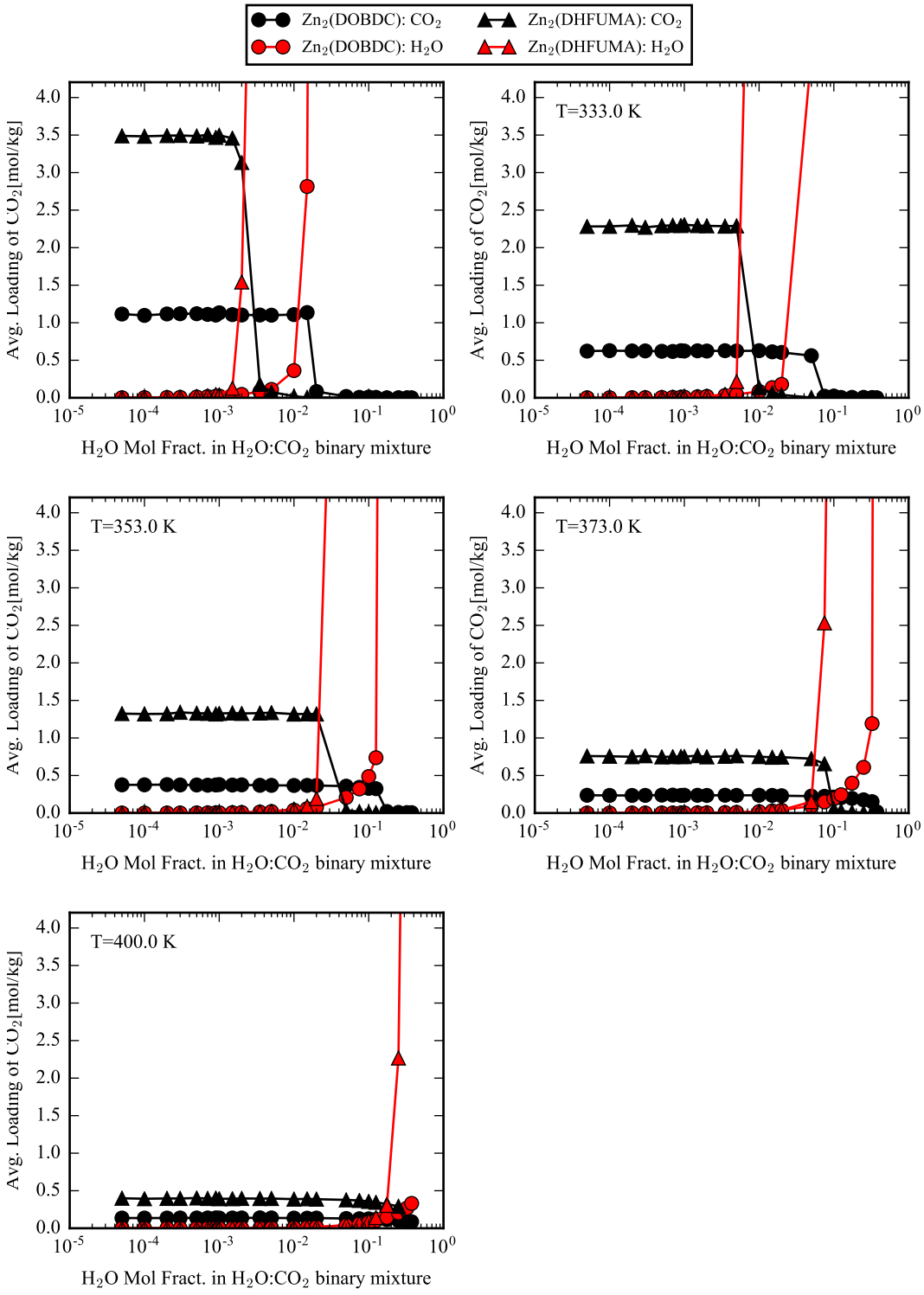

Figure S21: H_2O:CO_2 mixture analysis for all Zn analogs. Each data point corresponds to one GCMC simulation at P_{total} = 0.15 bar and each subplot corresponds to a fixed temperature of T = 313, 333, 353, 373, or 400 K where the molar composition of the H_2O:CO_2 mixture is varied.

Improvements in raw material costs

A significant advantage of the M_2(DHFUMA) analog series is the drastically reduced raw materials cost (RMC) in comparison to the M_2(DOBDC) series. A non-bulk order price quote from Sigma Aldrich yields a cost of \$466.0/100g of ligand for DHFUMA which is significantly cheaper in comparison to the \$2412/100g of DOBDC [*http://www.sigmaaldrich.com*, accessed 8 August 2016]. This ligand RMC cost dominates the expense of the metal source, where prices range from \$26.35/100g for $MgCl_2$ to \$65.00/100g $NiCl_2$ (again taken from non-bulk order price quotes from Sigma Aldrich). As we have predicted the increased H_2 volumetric storage potential in Mg_2(DHFUMA) (see Figure 2 in the main article) and the pareto optimality of all M_2(DHFUMA) analogs over their DOBDC counterparts for CO_2 selectivity in the presence of H_2O (see Figure 8 in the main article), we predict the DHFUMA analog series to be a cheaper, higher performing nanoporous material than M_2(DOBDC) for H_2 storage and CO_2 capture from wet flue gas if it can indeed be synthesized.

Proposed CO_2 capture process with M_2(DHFUMA)

We graphically illustrate a simple scheme for how one might design an industrial adsorption process if one of the top performing DHFUMA analogs were to be used for CO_2 capture from a mixture of N_2/CO_2 with non-trace amounts of H_2O. Figure S22 provides a general overview for how DHFUMA could be incorporated into an industrial scale CO_2 capture process from a coal-fired power plant flue stream. Figure S22(a) shows how a zeolite bed could be used to dry the flue gas to a permissible water content for DHFUMA while CO_2 adsorption occurs in the subsequent DHFUMA bed at high temperature. Desorption is illustrated in Figure S22(b) whereby the zeolite bed is heated to a high-temperature to desorb H_2O, and this desorbed water stream is cooled down just below the necessary temperature to condense in DHFUMA and thereby desorb CO_2. The ultimate result is a qualitative picture of how CO_2 capture might be performed at an industrial scale. The final amount of CO_2 captured and the amount of zeolite needed to dry the breakthrough of the stream to the minimum necessary water content would be optimized based upon experimental pilot-scale results that mimic the results of the section on "Optimizing CO_2 capture in binary CO_2:H_2O mixtures".

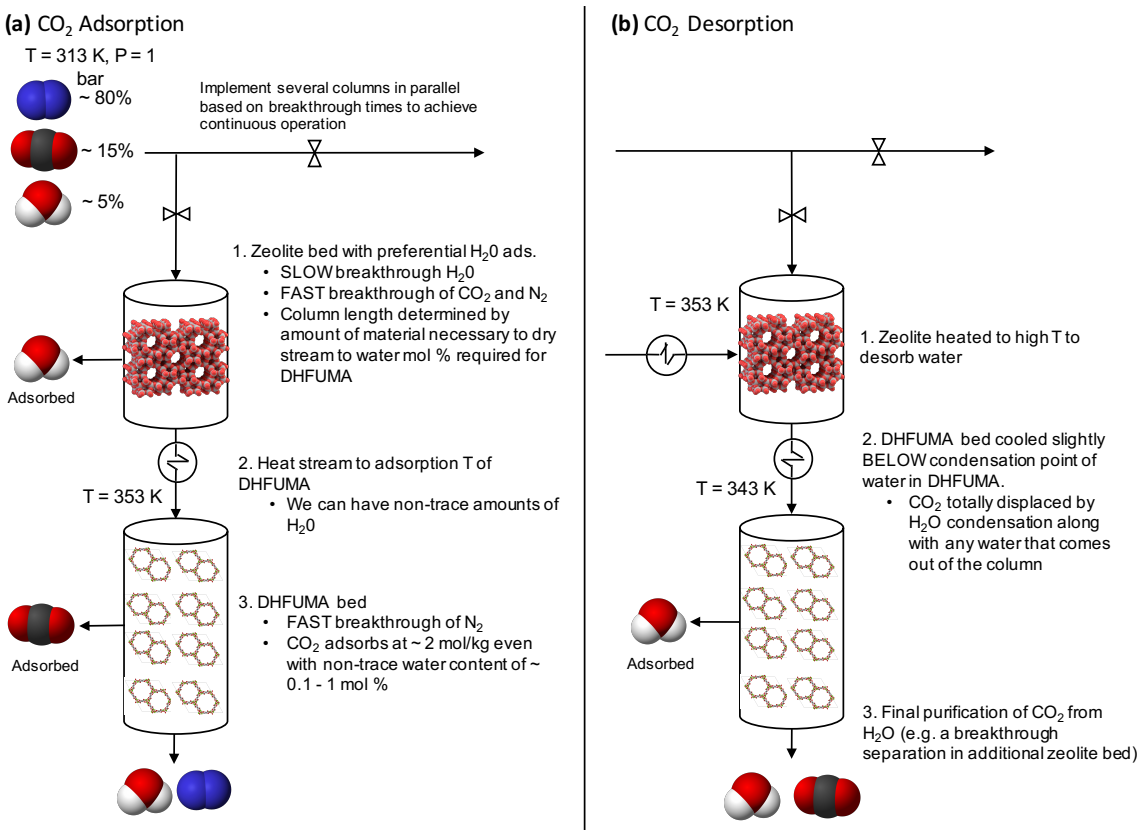

Figure S22: (a) CO_2 adsorption. A cheap zeolite bed is utilized to reduce the water content to the maximum threshold for the DHFUMA bed, and high temperature adsorption of CO_2 occurs. (b) CO_2 desorption. The water that was orginally adorbed by the first zeolite bed is used to desorb the strongly bound CO_2 in the DHFUMA bed.

Attempted synthetic procedures

Our attempts to synthesize the family of M_2(DHFUMA) materials (where M: Zn(II) and Mn(II)) with conventional heating methods were not successful; it is thought that this is due to the high reactivity of the dihydoxyfumaric acid (DHFUMA) ligand which tends to break down into oxalic acid or 1-hydroxy-methanetricarboxylic acid.

All chemicals were purchased from Sigma Aldrich ($Zn(NO_3)_2{\cdot}(H_2O)_6$, $Mn(NO_3)_2{\cdot}(H_2O)_4$ and dihydroxyfumaric acid hydrate) and used without further purification. A mixture of $Zn(NO_3)_2{\cdot}(H_2O)_6$ (0.029 g) and DHFUMA (0.015 g) in 4 mL of dimethylformamide (DMF) was sealed in a 12 mL scintillation vials and heated to 120 °C for 72 hours and then cooled to room temperature at a rate of 0.2 °C/min. Colorless hexagonal type crystals suitable for single crystal X-ray diffraction were obtained but structural analysis revealed that the formula of the material is based upon Zn(oxalate), shown in Figure S23a.[16] Under these specific conditions, the DHFUMA has converted into oxalate. Reactions of the same reactants at lower temperature or for less time resulted in clear solutions without the formation of any product. The replacement of $Zn(NO_3)_2{\cdot}(H_2O)_6$ with $Mn(NO_3)_2{\cdot}(H_2O)_4$ (0.025 g) with DHFUMA (0.015 g) in DMF:EtOH (1:1) at 85 °C for 12 hours resulted also in the deconstruction of DHFUMA into oxalate and structural analysis of the single crystals revealed that the material is previously reported by Chan *et al.* shown in Figure S23b.[17] In order to exclude the possibility that DMF acts as a base and deconstructs DHFUMA, we have then performed reactions in H_2O or H_2O:EtOH mixture and adjusted the pH at ∼7 with NaOH 1M. We have also obtained crystals from the reaction of $Mn(NO_3)_2{\cdot}(H_2O)_4$ (0.025 g) and DHFUMA (0.015 g) in 4 mL of H_2O:EtOH (1:1), heated at 60 °C for 6 hours. However, in such conditions DHFUMA undergoes an aerial oxidation followed by a benzilic acid type rearrangement promoted by transition-metal cations. The resultant crystals were identified as manganese 1-hydoxy-methanetricarboxylate, previously reported by Abrahams *et al.* and shown in Figure S23c.[18] Relevant crystal data from the synthesized structures are shown in Table S6.

Table S6: Crystal data for structures obtained with the reactions of Zn(II) or Mn(II) and dihydroxyfumaric acid.

	Zinc oxalate	Manganese oxalate·DMF	Manganese 1-hydroxymethane-tricarboxylate
Space group	C2/c	Pbcn	I-43m
a [Å]	31.89(3)	15.2245(7)	15.25247(5)
b [Å]	16.274(16)	7.8639(3)	15.25247(5)
c [Å]	9.301(9)	10.1198(4)	15.25247(5)
α [°]	90	90	90
β [°]	93.18(3)	90	90
γ [°]	90	90	90
V [Å^3]	4819(8)	1211.58(9)	3548.30(2)

Based on these observations, we could state that DHFUMA is not stable under the reaction conditions we used and it precludes the formation of the desired structure. Our efforts now are focused on applying alternative synthetic strategies (microwave and combinatorial synthesis, and two layers diffusion at room temperature) in order to better understand the reactivity of DHFUMA and so we can have access to this family of M_2(DHFUMA) materials and experimentally study their properties. Finally, we summarize the ligand modifications that occur under various reaction conditions in Figure S24.

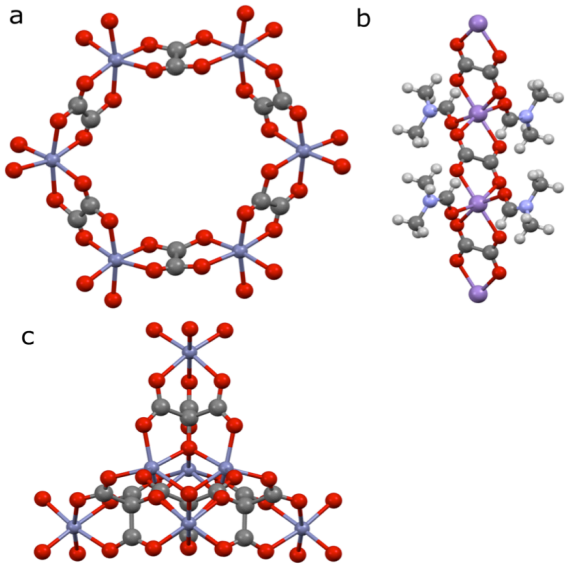

Figure S23: Schematic illustration on how the dihydroxyfumaric acid transforms under specific conditions.

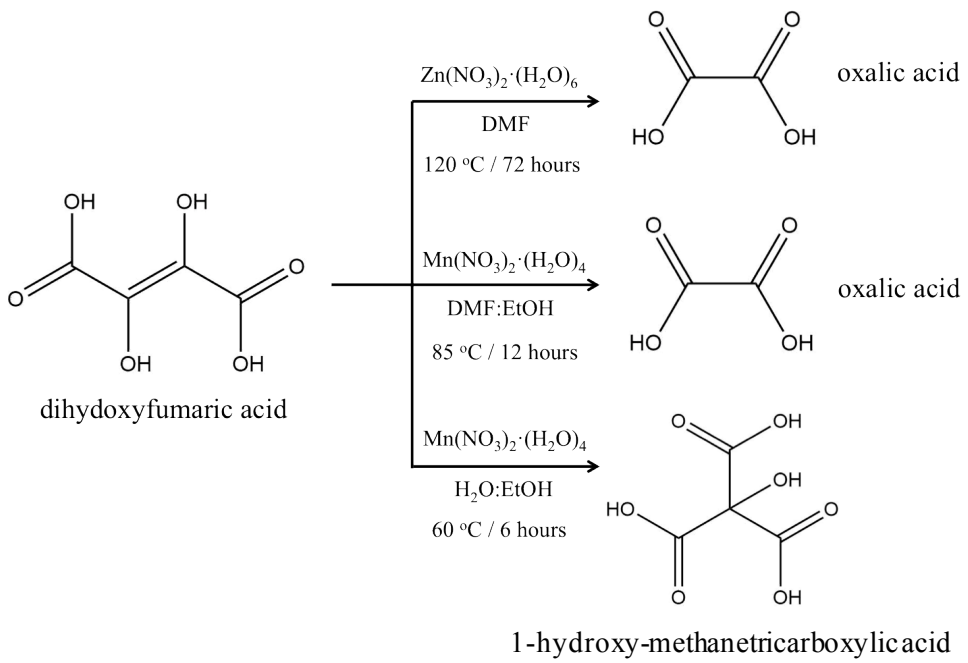

Figure S24: Schematic illustration on how the dihydroxyfumaric acid transforms under specific conditions.

References

(1) VandeVondele, J.; Hutter, J. Gaussian Basis Sets for Accurate Calculations on Molecular Systems in Gas and Condensed Phases. *J. Chem. Phys.* **2007**, *127*, 114105.

(2) Goedecker, S.; Teter, M.; Hutter, J. Separable Dual-Space Gaussian Pseudopotentials. *Phys. Rev. B* **1996**, *54*, 1703.

(3) Krack, M. Pseudopotentials for H to Kr Optimized for Gradient-Corrected Exchange-Correlation Functionals. *Theor. Chem. Acc.* **2005**, *114*, 145–152.

(4) Guidon, M.; Hutter, J.; VandeVondele, J. Auxiliary Density Matrix Methods for Hartree- Fock Exchange Calculations. *J. Chem. Theory Comput.* **2010**, *6*, 2348–2364.

(5) Spencer, J.; Alavi, A. Efficient Calculation of the Exact Exchange Energy in Periodic Systems Using a Truncated Coulomb Potential. *Phys. Rev. B* **2008**, *77*, 193110.

(6) Perdew, J. P.; Burke, K.; Ernzerhof, M. Generalized Gradient Approximation Made Simple. *Phys. Rev. Lett.* **1996**, *77*, 3865.

(7) Adamo, C.; Barone, V. Toward Reliable Density Functional Methods Without Adjustable Parameters: The PBE0 Model. *J. Chem. Phys.* **1999**, *110*, 6158–6170.

(8) Ernzerhof, M.; Scuseria, G. E. Assessment of the Perdew–Burke–Ernzerhof Exchange-Correlation Functional. *J. Chem. Phys.* **1999**, *110*, 5029–5036.

(9) Grimme, S.; Antony, J.; Ehrlich, S.; Krieg, H. A Consistent and Accurate Ab Initio Parametrization of Density Functional Dispersion Correction (DFT-D) for the 94 Elements H-Pu. *J. Chem. Phys.* **2010**, *132*, 154104.

(10) Boys, S. F.; Bernardi, F. d. The Calculation of Small Molecular Interactions by the Differences of Separate Total Energies. Some Procedures With Reduced Errors. *Mol. Phys.* **1970**, *19*, 553–566.

(11) Born, M. On the Stability of Crystal Lattices. I. *Math. Proc. Cambridge Philos. Soc.* **1940**, *36*, 160–172.

(12) Mouhat, F.; Coudert, F. m. c.-X. Necessary and Sufficient Elastic Stability Conditions in Various Crystal Systems. *Phys. Rev. B* **2014**, *90*, 224104.

(13) Pham, T.; Forrest, K. A.; Mclaughlin, K.; Eckert, J.; Space, B. Capturing the H_2-Metal Interaction in Mg-Mof-74 Using Classical Polarization. *J. Phys. Chem. C* **2014**, *118*, 22683–22690.

(14) Mercado, R.; Vlaisavljevich, B.; Lin, L.-C.; Lee, K.; Lee, Y.; Mason, J. A.; Xiao, D. J.; Gonzalez, M. I.; Kapelewski, M. T.; Neaton, J. B. et al. Force Field Development From Periodic Density Functional Theory Calculations for Gas Separation Applications Using Metal-Organic Frameworks. *J. Phys. Chem. C* **2016**, *120*, 12590–12604.

(15) Peng, X.; Lin, L.-C.; Sun, W.; Smit, B. Water Adsorption in Metal–Organic Frameworks With Open–Metal Sites. *AIChE J.* **2015**, *61*, 677–687.

(16) Evans, O. R.; Lin, W. Synthesis of Zinc Oxalate Coordination Polymers via Unprecedented Oxidative Coupling of Methanol to Oxalic Acid. *Cryst. Growth Des.* **2001**, *1*, 9–11.

(17) Chan, Y.-N.; Zhao, H.-K.; Wang, X.-G.; Zhao, X.-J. Catena-Poly[[bis(N,N-Dimethylformamide)manganese(II)]-Di-μ2-Oxalato]. *Acta Crystallogr., Sect. E: Struct. Rep. Online* **2007**, *63*, m70–m72.

(18) Abrahams, B. F.; Hudson, T. A.; Robson, R. In Situ Synthesis of Trisubstituted Methanol Ligands and Their Potential as One-Pot Generators of Cubane-Like Metal Complexes. *Chem. Eur. J.* **2006**, *12*, 7095–7102.